Estimating UV-B, UV-Erithemic, and UV-A irradiances from global horizontal irradiance and MERRA-2 ozone column information

Agustín Laguarda [1]
Laboratorio de Energía Solar
Facultad de Ingeniería,
Universidad de la República (Udelar),
Montevideo, 11700 Uruguay
email: agu.laguarda@gmail.com

Gonzalo Abal
Laboratorio de Energía Solar
CENUR LN,
Udelar, Salto, 50000 Uruguay

Paola Russo
Laboratorio de Energía Solar
CENUR LN,
Udelar, Salto, 50000 Uruguay

Aron Habte
National Renewable Energy Laboratory,
Colorado, USA.

The ground ultraviolet (UV) solar radiation is relevant due to its impacts on plastics degradation (mainly UVA) and on human health (UVB and erithemic UV, or UVE). UV ground measurements are not as ubiquitous as the relatively common global horizontal irradiance (GHI) measurements. Three simple models that estimate the UVA, UVB, and UVE components of solar irradiance from GHI and ozone column information are locally adjusted and validated. Five 1-minute datasets from three sites in southeastern South America and two in the United States are used for simultaneous solar irradiance and UV data. All sites correspond to temperate midlatitude regions. Simultaneous atmospheric total ozone column information is obtained from the reanalysis Modern-Era Retrospective analysis for Research and Applications (MERRA-2) database for each site. Aside from locally adjusted models, average models with a single set of coefficients are also evaluated. For instance, the best average model is able to estimate UVE with a typical uncertainty below 12% and mean biases between ±3%, relative to the average of the measurements. Similar results are reported for the UVB and UVA components. These results, which can be useful in regions with similar climate and geography, provide a simple way to estimate UV irradiance under all-sky conditions with known uncertainty. This is an alternative to global satellite-based UV estimates, which can have high uncertainties at specific locations. Because MERRA-2 information has a global coverage, when coupled with good satellite-based estimates for GHI, UV irradiances can be estimated by this method over a large territory.

Keywords: environmental UV radiation, UVA, UVB, UVE, solar radiation modeling

1 Introduction

An adequate understanding of the ultraviolet solar radiation (UV) at the Earth's surface is important mainly due to its effects on exposed biological organisms. It can have negative impacts on human health, inducing sunburns, premature skin aging, eye damage, and an increased risk of skin cancer [1,2], and these effects depend on the accumulated dosage. The environment can also be affected by UV radiation (ecosystem degradation), and it can also cause economic impacts by degrading exposed materials and equipment [3]. This is especially applicable to the transparent cover (inclusive of coatings) and encapsulant of photovoltaic (PV) modules [4].

Solar UV radiation is categorized into sub-bands according to its effects on biological tissues: UVA (315–400 nm) and UVB (280–315 nm). The incident UV irradiance (280–400 nm) weighted by the average human skin response standard spectrum [5,6] is the erythemic UV or UVE, and it is the basis for the UV index calculation used for public reports on UV irradiance levels.

The most reliable way to obtain UV information for any sub-band is based on ground measurements; however, due to the scarcity of such measurements, it is convenient to have models with known uncertainties to estimate these components. Surface UV can be modeled using relevant information retrieved by meteorological satellites, such as atmospheric ozone content, aerosols, and cloud cover, combined with surface reflectivity data. Satellite observations are particularly useful for this purpose because they provide efficient coverage of large geographic areas and almost near real-time information over long periods.

By using information from these models, it is possible to capture the spatial distribution and temporal variability of climatic and meteorological patterns regarding UV. For instance, the UV-Index Operating System (UVIOS) uses information from the Meteosat Second Generation and Meteorological Operational Satellite-B to retrieve near-real-time and short-term forecasting of UV radiation over Europe at a spatial resolution of 5 km and a temporal resolution of 15 minutes [7]. This operational approach, based on radiative transfer calculations, can provide reasonably accurate UV estimates. However, it requires substantial computational resources to handle the large volumes of satellite real-time data, justifying the need for efficient and scalable modeling techniques.

An efficient alternative approach involves using measured or estimated broadband global horizontal irradiance (GHI, in W/m^2) as a basis to estimate UV radiation components. Reliable measurements of GHI are relatively common, and several accurate models and databases provide GHI estimates from satellite information. Geostationary satellites provide valuable data on cloudiness, which significantly impacts solar radiation. GHI models utilize this satellite information, along with other ancillary data, to account for the effects of clouds and atmospheric conditions on solar radiation. A common approach involves first estimating GHI under clear sky conditions and then adjusting for cloud effects using geostationary satellite data [8–10]. Among various alternatives for GHI, there is the National Renewable Energy Laboratory's (NREL) National Solar Radiation Data Base (NSRDB, [11]), which primarily

---

[1] Corresponding Author.
Version 1.18, July 28, 2024

focuses on the Americas, and the Copernicus Atmosphere Monitoring Service (CAMS) Radiation Service [12], which relies on the Heliosat-4 model [9], covering mainly Europe and Africa.

A viable straightforward two-step scheme to estimate UV components from satellite information consists of (i) estimating GHI from a suitable satellite model and (ii) applying a simple parameterization to transform GHI to UV irradiance in the corresponding sub-band. This involves adding ozone information. In this work, we focus on the second step of this procedure, using GHI measurements instead of satellite-based estimates to assess several simple parametrizations for each UV band. As a result, we obtain an accurate and fast method for estimating each UV component from GHI and ozone total content information obtained from a publicly available source.

In this context, a relevant dimensionless quantity is the UV fraction for each sub-band, shown in Eq. (1):

$$f_A = \frac{UVA}{GHI}, \qquad f_B = \frac{UVB}{GHI} \quad \text{and} \quad f_E = \frac{UVE}{GHI}. \qquad (1)$$

The UV fractions are most sensitive to variations in the solar altitude (or relative air mass), cloudiness, and stratospheric ozone content in the case of the shorter wavelengths. In a previous work [13], several models for the UV fractions were tested against a limited ground data set. Among these, the power model (PM), shown in Eq. (2), stood out for its simplicity and good accuracy for all UV bands. The main objective of this work is to train and assess the performance of the PM parametrization, with a focus on the f_B and f_E fractions. For clarity, results for the UVA fraction are included in Appendix A. In this work, a greater amount of quality simultaneous UV and GHI data (five sites, covering a greater portion of the subtropical American continent) is used, and all data are resampled at the 10-minute level, which is the time step used by the Geostationary Operational Environmental Satellites (GOES) that have observed this region since 2018. For comparison, a polynomial model based on the one used by NREL is also included (named NP in this work). The original NP model for UV fraction [14] is a fourth-order polynomial in air mass obtained as a result of radiative transfer simulations, specifically designed for total UV radiation (280–400 nm). It focuses on the full UV range, instead of specific ranges like UVA or UVB like this work, because it is related to the UV radiation exposure for PV materials.

In this work, we consider an extended version of the polynomial model for each UV band, incorporating ozone as a predictor, as shown in Eq. (3). Ozone strongly absorbs shortwave ultraviolet radiation up to about 320 nm, mainly in the Hartley and Huggins bands, and has a negligible effect on the UVA sub-band [15]. In Figure 1, the ozone absorption cross-section in the UV spectrum is shown. The Hartley and Huggins bands significantly contribute to the absorption of solar UV radiation, particularly in the UVB and UVE ranges. Therefore, the f_B and f_E models must consider ozone [13]. As a baseline model, a constant UV fraction, Eq. (4), is also adjusted and tested.

Power model (PM):

$$f_X = a_0\, k_t^{a_1} \times m^{a_2} \times [O_3]^{a_3}, \qquad (2)$$

Polynomial model (NP):

$$f_X = b_0 + b_1 m + b_2 m^2 + b_3 m^3 + b_4 m^4 + b_5 [O_3] + b_6 [O_3]^2, \quad (3)$$

Constant model (CT):

$$f_X = c_0. \qquad (4)$$

where X stands for each sub-band (A, B, E), $k_t = GHI/S_0 \cos(z)$ is the clearness index (a normalized version of GHI with S_0 the solar irradiance at the top of the atmosphere and z the solar zenith angle), and $[O_3]$ is the ozone column in Dobson units (DU). Since

Ozone dependence is not expected to be relevant for the UVA band, versions of NP and PM without this dependence are also considered and labeled NP0 ($b_5 = b_6 = 0$) and PM0 ($a_3 = 0$), respectively.

In order to adjust the models to local data, representative sets of GHI and UVX pairs are required. In addition, the estimation of UVB and UVE requires simultaneous Ozone column information at each site. Five sites with different climates are used, as described in the next Section. The spatial variability of the locally adjusted coefficients is important. If it is low, an average model with a single set of coefficients may be useful to provide UV information over sites with similar climatic characteristics, so this possibility will also investigated.
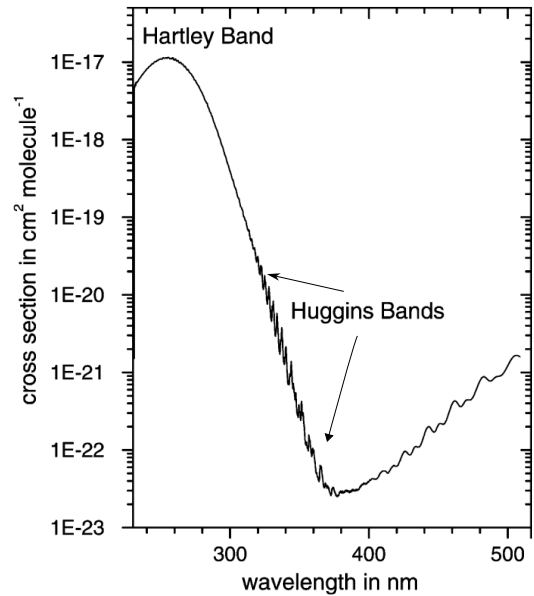

Fig. 1 Ozone absorption cross-sections spectrum at 293 K, presented on a logarithmic scale. The Hartley and Huggins bands are indicated. Adapted from [16]

2 Information base

2.1 Ground measurements. To validate and train the proposed models, measurements at ground level from five different places are used. The five measurement sites are located in subtropical climates in South and North America. Table 1 presents the detailed locations, the reference codes used, and their Köppen Geiger climate classifications [17]. At all sites, GHI is simultaneously measured along with at least one component of UV radiation. The instrumentation used, the frequency of recorded measurements and the period of measurement are listed in Table 2.

Periodic maintenance, including calibration of the instruments, is the responsability of the operators at each site listed in Table 1. At LES (Laboratorio de Energía Solar, Uruguay http:les.edu.uy) the GHI instruments are calibrated at the laboratory at 2-year intervals with technical trazability to the World Radiometric Reference (WRR) in PMOD, Switzerland. The UV instrument participated in a international intercomparison held by the World Meteorological Organization (WMO) at Buenos Aires, Argentina in 2018. The ATM site is run by INUMET, the national meteorological service from Uruguay. Both instruments at this site where new had factory calibrations from 2019. The GCO site is part of the Baseline Measurement System (BMS) of the NREL experimental facility in Golden, Colorado [18], with instruments calibrated at 1-year intervals[2]. The GWN site is part of the Surface Radiation Budget

---

[2]As detailed in https://midcdmz.nrel.gov/apps/html.pl?site=BMS;page=

Table 1   Measurement sites-information, including updated Köppen Geiger climate classification [17].

Site location	Code	Operator	Lat (°)	Lon (°)	Alt (m)	Climate
Salto, Uruguay	LES	LES	-31.28	-57.92	56	Cfa
Atlántida, Uruguay	ATM	INUMET	-34.78	-55.75	11	Cfa
Golden, Colorado, USA	GCO	NREL-BMS	+39.74	-105.18	1829	Dfb
Goodwin Creek, Mississippi, USA	GWN	SURFRAD	+34.25	-89.87	98	Cfa
Pilar, Córdoba, Argentina	PIL	SAVER-NET	-31.68	-63.87	330	Cfa/Cwa

(SURFRAD) network operated by the National Oceanic and Atmospheric Administration (NOAA)[3]. The PIL site is maintained by the SAVER-NET network[4], a tri-national colaboration between Argentina, Chile and Japan that maintains measurements of UV global irradiance at various locations. PIL is located near the city of Cordoba, Argentina, and it was selected for this work because it had a good local maintenance schedule. Both instruments at this site had factory calibrations from 2018 and participated in the WMO sponsored international intercomparison at Buenos Aires, Argentina in 2018.

2.2   Quality control of ground measurements. The next step in this project is to use the best UV models to estimate UVX from satellite-based GHI over mid-latitudes over America, so we select a time step of 10 minutes because this is the frequency of the geostationary satellite images (currently GOES-16). As a first step, all 1-min ground data are averaged to 10-minute intervals.

For training and validating the models, it is necessary to use well-behaved, typical data and exclude as much as possible infrequent, atypical measurements. A quality control procedure was applied to the ground GHI and UV measurements to filter extreme values. We refer the reader to Appendix B for the details of the applied filters and their results on each site and data pair (GHI, UVA; GHI, UVB; and GHI, UVE). The filters for GHI imply lower and upper bounds as recommended by the Baseline Surface Radiation Network (BSRN) [19]. Filters for UV are reasonable bounds for these variables, as discussed in Appendix B. Typical UVE fractions tend to decrease with air mass and increase with solar irradiance, as shown in Figure 2. Lower and upper bounds also applied to UV fractions, as described in Appendix B. The results of the filtering procedure are summarized in Table 3, for each site and the relevant variable pair. The initial records are those with solar altitudes, α_s, greater than 7°, thus excluding measurements with high air masses and low sun altitudes, for which directional (cosine) errors can be large. Finally, only complete data pairs are listed in Table 3 because these are required for training and evaluating the models.

As Table 3 shows, less than 5% of the the available high sun records are discarded at each site by the quality control procedures detailed in Appendix B.

2.3   Ozone information. The ozone present in the stratosphere plays an important role in the attenuation of the lower wavelengths of the solar spectrum, as stated before and shown in Figure 1. In this work, the total ozone column, $[O_3]$, in Dobson units (DU), is used as one of the predictors for these UV fractions. This information is obtained from the National Aeronautics and Space Administration's Modern-Era Retrospective analysis for Research and Applications (MERRA-2) reanalysis database [20], based on the Global Earth Observing System Version-5 (GEOS-5) numeric atmospheric model. It provides a wide spectrum of meteorological variables over the entire globe at hourly steps, from 1980–present, with a spatial resolution of 0.5° × 0.625°. Due to its construction, it does not present temporal or spatial gaps, which makes it suitable as input for a UV-based radiation satellite model. In [21], daily averages of MERRA-2 ozone estimates were compared with spectrophotometer-based ozone ground measurements for one site

(a) Dependence on air mass

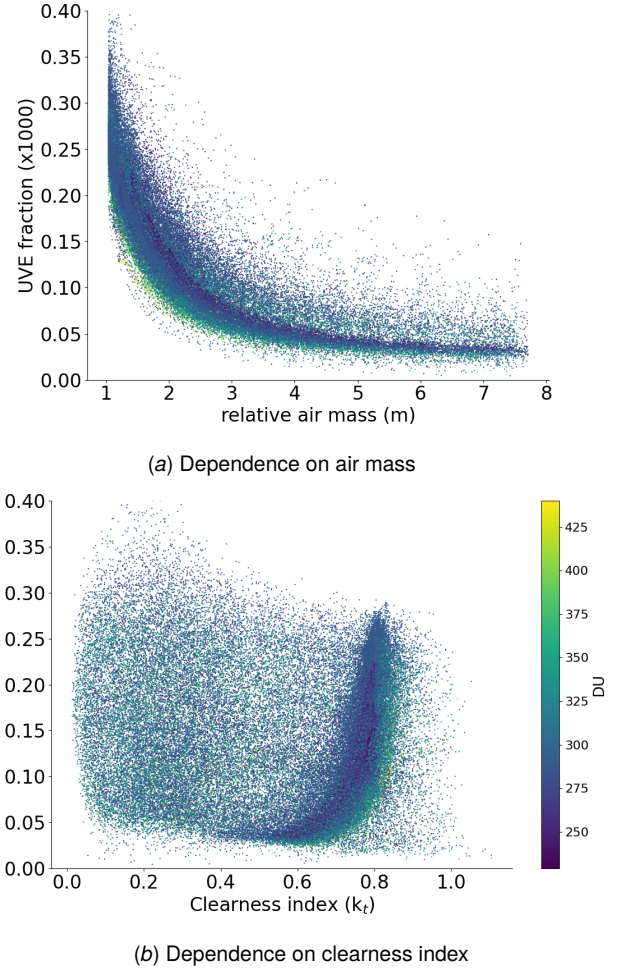(b) Dependence on clearness index

Fig. 2   UVE fraction data for the GCO site. The color denotes the ozone content in Dobson units. As shown, the greater the ozone content, the lower the f_E.

in Uruguay over several years. A good performance with rMBD of +2.0% and a rRMSD of 2.4% was found. The hourly information ensures that the short-term variations in ozone concentration are accurately captured, providing more precise inputs for the UV model. Finally, ozone has been linearly interpolated to 10-minute intervals for use in this work.

3   Methodology

The nontrivial UVB and UVE fraction models, Eqs. (2) and (3), use air mass, m, clearness index, k_t (defined below), and the ozone concentration, $[O_3]$, as predictors. These predictors account for the sun's beam path length across the atmosphere, cloudiness, and ozone column, respectively. The air mass depends on the apparent sun position and is calculated from the time tag and location at the center of the 10-minute interval using the expression provided by [22]. In essence, this geometric variable describes the ratio between the actual optical path of the solar beam and the

_____
instrumes.

Table 2 Measurements and instruments available at each site. KZ stands for the Kipp & Zonen instrument manufacturer. The last columns show the time interval between recorded measurements and the time period over which the data was measured. The site codes and operators are listed in Table 1.

Site	GHI	UVA	UVB	UVE	Frequency (min^{-1})	Period
LES	KZ CMP10	KZ UVS-A-E	-	KZ UVS-A-E	1	01/2018 – 12/2021
ATM	KZ CMP6	-	KZ UVS-B	-	1/10	02/2021 – 12/2021
GCO	Eppley PSP	KZ UVS-A-T	KZ UVS-B-T	KZ UVS-E-T	1	08/2018 – 12/2021
GWN	Spectrolab SR-75	-	-	Yankee UVB1	1	07/2018 – 12/2021
PIL	KZ CMP6	KZ UVS-A-T	-	KZ UVS-E-T	1	07/2017 – 12/2021

Table 3 Number of 10-minute records in each data set after quality control. In parenthesis, the percentage relative to the available records with high sun (i.e., above 7°). The last row aggregates data for all sites.

Site	$\alpha_s > 7°$	(GHI, UVA)	(GHI, UVB)	(GHI, UVE)
LES	61833 (100%)	59185 (95.7%)	-	59026 (95.5%)
ATM	19524 (100%)	-	19277 (98.7%)	-
GCO	79700 (100%)	78928 (99.0%)	78735 (98.8%)	78901 (99.0 %)
GWN	80634 (100%)	-	-	77765 (96.4%)
PIL	64903 (100%)	59644 (91.9%)	-	58431 (90.0%)
All sites		197757 (95.8%)	98012 (98.8%)	274123 (95.5%)

local vertical path. The Rayleigh scattering strongly attenuates UV radiation in relation to broadband radiation (shorter wavelength), and its effects depend on the air mass. The greater the air mass, the lower UV fraction, as shown for UVE in Figure 2(a). The clearness index, k_t, is the ratio of GHI and the solar irradiance incident at the top of the atmosphere. It is a dimensionless positive quantity (typically less than 1) that acts as a proxy for the effects of cloudiness on f_X. Typically, cloudiness tends to decrease UV fraction, as shown in Figure 2(b) for UVE. The ozone concentration has typical values between 250 and 400 DU and is scaled by a factor of 100 DU so that the ozone ratio renges from 2.5 to 4.0.

The usual performance metrics used in the solar assessment field are used to describe performance [23]: the mean bias deviation (MBD), the root mean square deviation (RMSD), and the Kolmogorov-Smirnov index (KSI). The first two are defined as:

$$\text{MBD} = \frac{1}{N} \sum_{i=1}^{N} d_i, \qquad \text{RMSD} = \left[\frac{1}{N} \sum_{i=1}^{N} d_i^2 \right]^{\frac{1}{2}} \qquad (5)$$

where N is the number of samples, and $d_i = \widehat{y_i} - y_i$ are the residuals from the modeled estimates (for each UV sub-band) $\widehat{y_i} = GHI \times f_{UVX}$ compared to the measured UV irradiance, $y_i = \text{UVX}$. Both metrics (in W/m^2) express different aspects of the accuracy of a model evaluating data on a sample-to-sample basis. Relative versions of these indicators, rMBD and rRMSD, are expressed as percentages of the average of the reference values.

The KSI [24] is a measure of the statistical similarity between the estimates ($\hat{F}$) and the reference (F) cumulative probability functions across the range of the target variable y:

$$\text{KSI} = \int |\hat{F}(y) - F(y)| \, dy. \qquad (6)$$

KSI is positive and also has irradiance units, with lower KSI values indicating more statistical similarity between the two datasets. Although a low rRMSD value could also correspond to a low KSI value, the two metrics measure different aspects of the model's performance.

The coefficients for the UV fraction models, Eqs. (2) to (4), are obtained using the `curve_fit` function of Python's module `scipy.optimize` to optimize the UVX radiation output accuracy. A standard random sampling and cross-validation technique is used, where each dataset is randomly separated into training and validation subsets, each with half the data. After 500 iterations, average parameters and performance indicators are obtained. The same procedure is separately applied to each site and variable pair,

according to the available data after quality control, as listed in Table 3. This produces locally adjusted models for each site and variable, as listed in Table 4 and Table 5 for UVE and UVB, respectively. The locally adjusted coefficients for the UVA models can be found in Table 8. To obtain a unique f_X parametrization for each UV sub-band, a spatially weighted average of the local coefficients from each site, s, is performed, $< x >= \sum w_s x_s$. The weights, w_s, for each site are proportional to the number of data pairs from each site, N_s: $w_s = \frac{N_s}{\sum N_s}$. The average coefficients for each site and their corresponding standard deviations are listed in the corresponding tables for each variable. The performance of these "average" models is then evaluated at each site.

Note that we chose sites with similar climate classifications (see Table 1), so the average models are expected to perform reasonably well over midlatitude temperate sites. However, no claim of universality of the results can be made, and these models may not be applicable to tropical, polar, or extremely high-altitude regions without further adjustments. For application in such conditions, local calibration of the UV fraction coefficients (Eq. (2)) with regional data is highly recommended.

4 Results and discussion

The absolute performance indicators (MBD and RMSD) in mW/m^2 for UVE are shown in Figure 3 for four sites. The measured averages are shown for each site, but the inter-site comparisons are made in absolute terms. The localized versions of the models (filled color bars) perform slightly better than the average models (hatched bars), as expected. The constant model (CT) for the UVE fraction is clearly inadequate, showing that its dependence on atmospheric conditions cannot be ignored. The NP and NP0 models differ only in the ozone dependence, which is present in the NP (blue) but absent in the NP0 (green). Ozone improves the model dispersion at all sites, as indicated by lower RMSDs. The best model is the PM, with RMSDs less than 8 mW/m^2.

Similar results are obtained for UVB, as shown in Figure 3 for two sites. Ozone improves the NP performance, as measured by RMSD, and the best local model is the PM, with RMSDs less than 70 mW/m^2. The inclusion of an easily accessible quantity as the total ozone content from MERRA-2 in the polynomial approach (NP) implies a performance gain reducing, on average, 2% of the rRMSD metric while slightly improving the relative bias for UVE (3% in the case of UVB). Thus, from now on, the NP variant with ozone will be considered for UVE and UVB. As expected, using ozone information provides no improvement for the UVA variable.

Table 4 Coefficients per site for UVE models (note the scaling factors). The last three columns show the average coefficients, their standard deviation, σ, and the relative variation, $\Delta = 100 \times \sigma/|x|$, a measure of the variability across sites. The last two rows indicate the number of data pairs and the corresponding weights.

Model	Coefficient	LES	GWN	GCO	PIL	Average x	σ	Δ (%)
CT	$c_0 \times 10^3$	0.208	0.184	0.180	0.198	**0.191**	0.013	6.8
NP	$b_0 \times 10^3$	1.117	0.986	0.839	1.409	**1.062**	0.243	22.9
	$b_1 \times 10^3$	-0.515	-0.762	-0.546	-0.696	**-0.632**	0.119	18.8
	$b_2 \times 10^3$	0.195	0.304	0.193	0.270	**0.241**	0.053	22.0
	$b_3 \times 10^4$	-0.321	-0.513	-0.304	-0.451	**-0.398**	0.101	25.4
	$b_4 \times 10^5$	0.189	0.305	0.173	0.266	**0.234**	0.063	26.9
	$b_5 \times 10^3$	-0.299	-0.083	-0.087	-0.392	**-0.197**	0.155	78.7
	$b_6 \times 10^4$	0.424	0.034	0.072	0.542	**0.237**	0.253	106.8
PM	$a_0 \times 10^3$	0.545	0.758	0.616	0.915	**0.705**	0.164	23.3
	a_1	-0.247	-0.201	-0.183	-0.206	**-0.207**	0.027	13.0
	a_2	-0.942	-1.435	-1.268	-1.277	**-1.247**	0.207	16.6
	a_3	-0.783	-1.020	-0.793	-1.237	**-0.950**	0.216	22.7
	# data pairs	59026	77765	78901	58431	-	-	-
	w_s	0.22	0.28	0.29	0.21	-	-	-
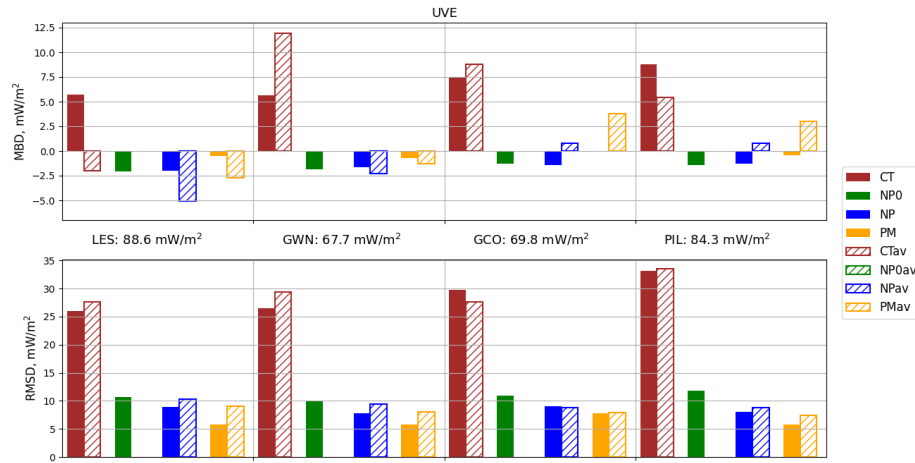
Fig. 3 Performance indicators (MBD and RMSD) for UVE models. The site-specific models (filled bars) use the coefficients from Table 4. The average models (hatched bars) use the average coefficients listed in the same table. The measurement average for each site is indicated between both panels.

Average models. The variation of the most significant coefficients across sites is small, as shown in Tables 4 et 5. For instance, the median of the percentage variations for UVE is less than 23%, and for UVB, it is 6.2%. This suggests that average models, based on a single set of average coefficients, could be useful for a broader region (midlatitude and similar climate sites).

For instance, the average versions of the PM models (PMave), using the average parameters listed in Tables 4 et 5 for UVE and UVB, are, respectively:

$$f_{UVE} = 0.705 \times 10^{-3} \cdot k_t^{-0.207} \cdot m^{-1.247} \cdot [O_3]^{-0.950}, \quad (7)$$

$$f_{UVB} = 0.523 \times 10^{-2} \cdot k_t^{-0.234} \cdot m^{-1.144} \cdot [O_3]^{-1.002}. \quad (8)$$

The same procedure is used with the CT and NP models to build their average versions. The performance of these average models for estimating UVE and UVB has been analyzed for all available data pairs. Tables 6 et 7 show how these average models perform at each site. The corresponding average model for UVA is evaluated in Table 9.

The performance results for the three average UVE models are listed in Table 6, which includes each metric's spatial weighted

average and its spread as quantified by the standard deviation (two last columns). The CT model, included only as a benchmark, shows a variable and significant bias across sites: between -2.3% and 17.5%. The rMBD for the NP and the PM, which are ozone dependent, has a smaller range: between -5.8% and 1.2% for the NP and between -3.0% and 5.4% for the PM. The rRMSD metric for each model is similar across sites. The NP estimates show values between 10.4% and 13.8%, whereas the PM has lower values, between 8.8 and 11.8%. Clearly, the PM method has better accuracy across sites, as measured by rRMSD. The NP model has better KSI metrics at GWN and PIL.

Scatter plots between the UVE measurements and the corresponding (NP or PM average) estimates are shown in Figure 5 for the LES site. The density of samples is color coded (brighter colors represent higher densities). This shows the smaller dispersion of the PM estimates. For high UVE values, both models tend to overestimate the measurements, whereas they underestimate them at low UVE values.

The corresponding UVB results are listed in Table 7, where all the relative metrics show larger values than for UVE. Biases have mixed signs, but large magnitudes at some sites. Indicators
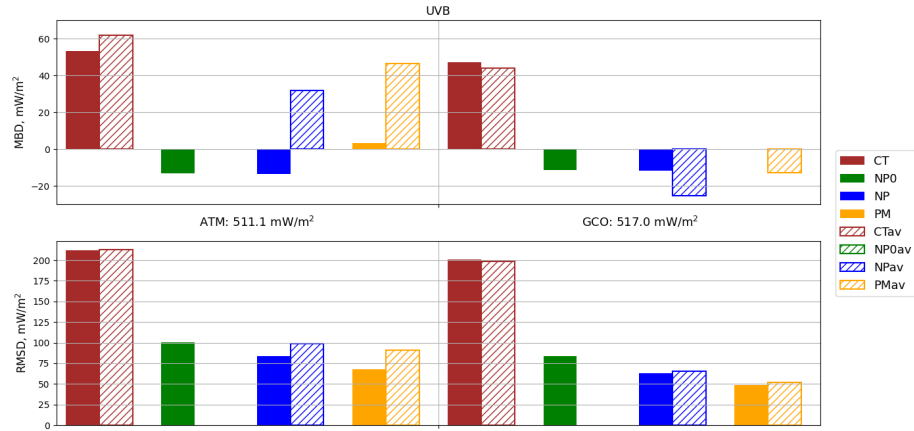
Fig. 4 Performance indicators (MBD and RMSD) for UVB models. The site-specific models (filled bars) use the coefficients from Table 5. The average models (hatched bars) use the average coefficients listed in the same table. The measurement average for each site is indicated between both panels. The PM model has a negligible bias at GCO.

Table 5 Coefficients per site for UVB models (note the scaling factors). The last three columns show the average coefficients, their standard deviation, σ, and the relative variation, $\Delta = 100 \times \sigma/|x|$, as a measure of their variability across sites. The last two rows indicate the number of data pairs and the corresponding weights for each site.

Model	Coefficient	ATM	GCO	Average	σ	Δ (%)
CT	$c_0 \times 10^2$	0.129	0.132	**0.131**	0.002	1.5
NP	$b_0 \times 10^2$	0.576	0.635	**0.623**	0.042	6.7
	$b_1 \times 10^2$	-0.316	-0.330	**-0.327**	0.010	3.1
	$b_2 \times 10^2$	0.104	0.113	**0.111**	0.006	5.4
	$b_3 \times 10^3$	-0.155	-0.172	**-0.169**	0.012	7.1
	$b_4 \times 10^5$	0.838	0.959	**0.935**	0.086	9.2
	$b_5 \times 10^3$	-0.740	-1.052	**-0.991**	0.221	22.3
	$b_6 \times 10^4$	0.484	1.084	**0.961**	0.424	44.1
PM	$a_0 \times 10^2$	0.495	0.530	**0.523**	0.025	4.8
	a_1	-0.303	-0.217	**-0.234**	0.060	25.6
	a_2	-1.215	-1.125	**-1.144**	0.064	5.6
	a_3	-1.029	-0.995	**-1.002**	0.024	2.4
	# data pairs	19277	78735	-	-	-
	w_s	0.20	0.80	-	-	-

at ATM are consistently larger than those at GCO, but almost 80% of the data pairs come from this last site and dominate the average model's performance. A qualitatively similar behavior to the UVE estimates can be observed: The average PM is more accurate than the NP, showing a lower dispersion (rRMSD) at each site and globally with 11.5% rRMSD (it was 10.7% for UVE). This small performance difference could be because the results for UVB are obtained from a smaller dataset with only two sites, which makes the average model less robust than the one for UVE. Figure 6 shows the scatter plots for the UVB estimates from the average NP and PM for the GCO site. Again, a greater dispersion of the estimates can be observed for the NP.

In summary, the PM has a better performance than the NP or the baseline CT model for all variables and sites considered, and it requires fewer coefficients (4) than the NP model (7). The average version of the PM is able to estimate either UVE or UVB with an approximate average dispersion of 11%. The applicability of this PM model is restricted to sites with similar climate conditions as those considered in this work (midlatitude, subtropical, temperate). The training of the coefficients to local UV data ensures that biases are kept small.

5 Summary and Conclusion

We considered the modeling of the UV fraction for the UVE, UVB, and UVA bands using three simple models: a constant model (CT), a polynomial model (NP), and a potential model (PM). These models depend on the clearness index (cloudiness), the air mass (describing the sun's apparent position), and the total ozone column. We also considered versions without ozone dependence. The models were fitted and evaluated using simultaneous 10-minute UV and broadband GHI data from 5 midlatitude sites through the Americas, all with temperate climates.

Except for the UVA band, ozone is required for modeling UVE and UVB with acceptable accuracy. For the regions considered, it is sufficient to use the ozone column estimates provided globally by the MERRA-2 database to significantly improve the performance indicators of the models.

The best model for UVE, PM, involves only four adjustable parameters. When locally adjusted, this model is able to predict the UVE fraction with dispersions between 7% and 11% of the average values and negligible biases (less than 0.5% in absolute terms), depending on the site. The average version of the PM model has

Table 6 UVE fraction models performance using spatially averaged coefficients over all sites. The number of data pairs and weights for each site is listed in Table 4. Relative metrics are expressed as a percentage of the average measured at each site. In the last columns, the weighted averages of the absolute metrics are included along with their standard deviations, σ, both expressed as percentages of the overall average measured irradiance, $77.7\,\mathrm{mW/m^2}$.

Model	Metric	LES	GWN	GCO	PIL	Mean	σ
	rMBD (%)	-2.3	+17.5	+12.6	+6.4	**+9.5**	8.5
CT	rRMSD (%)	31.2	43.3	39.5	39.7	**38.8**	5.1
	rKSI (%)	16.8	23.7	29.4	26.1	**23.6**	4.4
	rMBD (%)	-5.8	-3.4	+1.2	+1.0	**-1.7**	3.4
NP	rRMSD (%)	11.6	13.8	12.6	10.4	**12.3**	1.4
	rKSI (%)	7.4	3.2	3.6	2.1	**4.1**	2.9
	rMBD (%)	-3.0	-1.9	+5.4	+3.5	**+1.1**	4.1
PM	rRMSD (%)	10.3	11.8	11.3	8.8	**10.7**	1.3
	rKSI (%)	6.7	6.0	2.3	4.4	**4.7**	2.3
$\langle I_{UVE} \rangle$	(mW/m²)	88.6	67.7	69.8	84.3	77.7	9.0

Table 7 UVB fraction models performance using the averaged coefficients from Table 5 over all sites. In the last columns, the weighted averages of the metrics are included along with their standard deviations, σ, both expressed as percentages of the average measured irradiance shown in the last row.

Model	Metric	ATM	GCO	Mean	σ
	rMBD (%)	12.1	8.5	**9.2**	2.5
CT	rRMSD (%)	41.6	38.4	**39.0**	2.3
	KSI (%)	26.2	23.8	**24.3**	1.7
	rMBD (%)	6.2	-4.9	**-2.7**	7.8
NP	rRMSD (%)	19.3	12.6	**13.9**	4.7
	KSI (%)	6.5	4.6	**5.0**	1.3
	rMBD (%)	9.1	-2.5	**-0.2**	8.2
PM	rRMSD (%)	17.7	10.0	**11.5**	5.4
	KSI (%)	9.0	2.5	**3.8**	4.6
$\langle I_{UVB} \rangle$	(mW/m²)	511.1	517.0	515.8	4
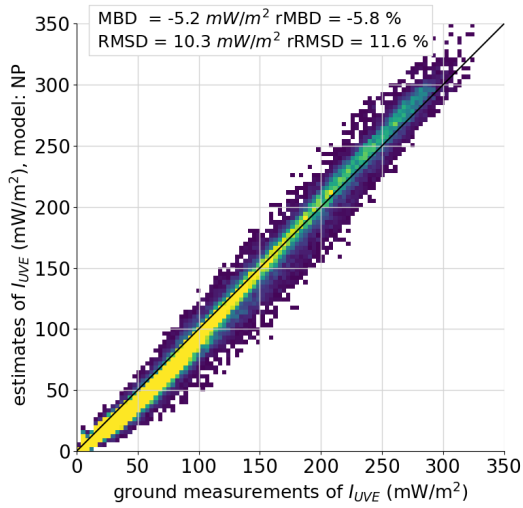
(*a*) NP (average)
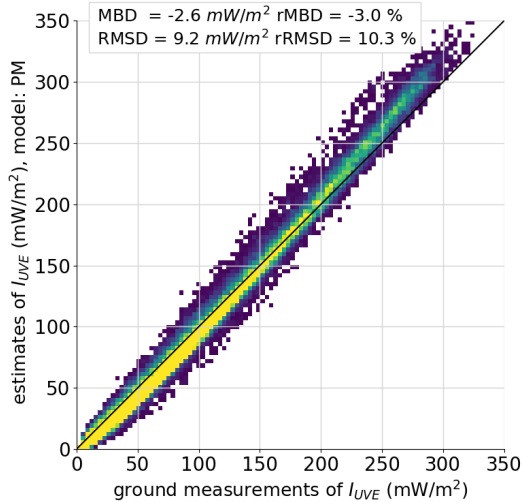
(*b*) PM (average)

Fig. 5 Scatter plots of UVE estimates from NP and PM average models for the LES site.

larger biases (reaching 5% at a site) but still acceptable rRMSD, less than 12% of the average values. The PM model is also best for UVB, although only two sites had this variable. The local versions are essentially unbiased and show dispersions between 10% and 13% of the average of the measurements. The average version has rRMSDs between 10% and 18%, poorer performance than for UVE. Thus, the PM provides a simple and precise parameterization for the UV fraction in both UVE and UVB bands.

We also considered UVA modeling, and the details are provided in Appendix A. Because ozone does not play a significant role in this band, versions without this dependence (NP0 and PM0) were locally adjusted. The PM0 model has three coefficients and a better performance than NP0 (five coefficients) at both sites. Its average version has an average rRMSD of 6.5% with negligible bias. This dispersion is similar to the average uncertainty assigned to both datasets.

In summary, the presented methodology can provide accurate information on UVA, UVB, and UVE solar irradiances under similar climatic conditions using Eq. (1) and the PM model, with the following inputs:

- Global horizontal irradiance (GHI)

- Total ozone content (except for UVA)

- Solar geometry

In this work, ground-measured GHI and ozone data from MERRA-2 were used, but any reliable GHI and ozone information source can be utilized. For application in different climatic areas, re-training the empirical coefficients of the PM model should be considered.

GHI is a ubiquitous variable, measured with good quality by most meteorological services at many sites worldwide. Additionally, ozone information is easily accessible through satellite or re-analysis data. Thus, this methodology provides a basis for characterizing UV radiation.
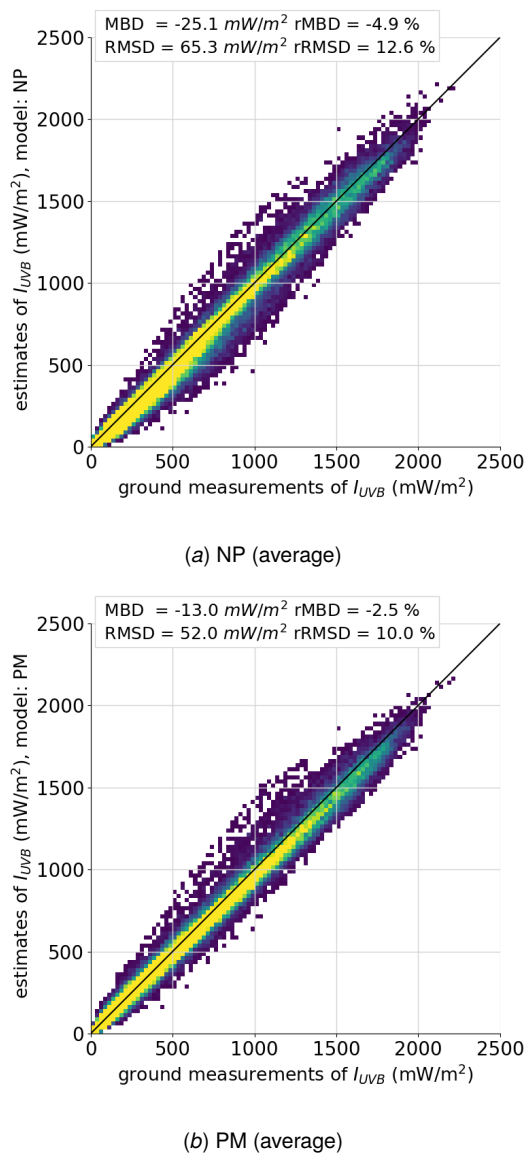
(a) NP (average)

(b) PM (average)

Fig. 6 Scatter plots of UVB estimates using NP and PM average models for the GCO site.

References

[1] Modenese, A., 2022, "Prevention of Health Risks Related to Occupational Solar Ultraviolet Radiation Exposure in Times of Climate Change and COVID-19 Pandemic," Atmosphere, **13**(7), p. 1147.

[2] Bojilova, R., Mukhtarov, P., and Miloshev, N., 2022, "Dependence of the Index of Biologically Active Ultraviolet Radiation on the Season and Time of Day," Atmosphere, **13**(9), p. 1455.

[3] Pickett, J. E., White, K. M., and White, C. C., 2018, "Chapter 1 - Service Life Prediction: Why Is This so Hard?" *Service Life Prediction of Polymers and Plastics Exposed to Outdoor Weathering*, C. C. White, K. M. White, and J. E. Pickett, eds., Plastics Design Library, William Andrew Publishing, pp. 1–18.

[4] Wohlgemuth, J. and Kurtz, S., 2014, "International PV QA Task Force's proposed comparative rating system for PV modules," National Renewable Energy Laboratory (NREL), Tech. Rep. NREL/CP-5J00-62846.

[5] International Organization for Standardization (ISO) and Commission Internationale de l'Eclairage (CIE), 2019, "Erythema Reference Action Spectrum and Standard Erythema Dose," Standard ISO/CIE 17166:2019(E), https://cie.co.at/publications/erythema-reference-action-spectrum-and-standard-erythema-dose-0

[6] Commission Internationale de l'Eclairage (CIE), 2014, "Rationalizing Nomenclature for UV Doses and Effects on Humans," World Meteorological Organization, WMO/GAW Report 211.

[7] Kosmopoulos, P. G., Kazadzis, S., Schmalwieser, A. W., Raptis, P. I., Papachristopoulou, K., Fountoulakis, I., Masoom, A., Bais, A. F., Bilbao, J., Blumthaler, M., Kreuter, A., Siani, A. M., Eleftheratos, K., Topaloglou, C., Gröbner, J., Johnsen, B., Svendby, T. M., Vilaplana, J. M., Doppler, L., Webb, A. R., Khazova, M., De Backer, H., Heikkilä, A., Lakkala, K., Jaroslawski, J., Meleti, C., Diémoz, H., Hülsen, G., Klotz, B., Rimmer, J., and Kontoes, C., 2021, "Real-time UV index retrieval in Europe using Earth observation-based techniques: system description and quality assessment," Atmospheric Measurement Techniques, **14**(8), pp. 5657–5699.

[8] Rigollier, C., Lefevre, M., and Wald, L., 2004, "The method Heliosat-2 for deriving shortwave solar radiation from satellite images," Solar Energy, **77**(2), pp. 159–169.

[9] Qu, Z., Oumbe, A., Blanc, P., Espinar, B., Gesell, G., Gschwind, B., Klüser, L., Lefèvre, M., Saboret, L., Schroedter-Homscheidt, M., and Wald, L., 2017, "Fast radiative transfer parameterisation for assessing the surface solar irradiance: The Heliosat-4 method," Meteorologische Zeitschrift, **26**(1), pp. 33–57.

[10] Laguarda, A., Giacosa, G., Alonso-Suárez, R., and Abal, G., 2020, "Performance of the site-adapted CAMS database and locally adjusted cloud index models for estimating global solar horizontal irradiation over the Pampa Húmeda region," Solar Energy, **199**, pp. 295–307.

[11] Sengupta, M., Xie, Y., Lopez, A., Habte, A., Maclaurin, G., and Shelby, J., 2018, "The National Solar Radiation Data Base (NSRDB)," Renewable and Sustainable Energy Reviews, **89**, pp. 51–60.

[12] Schroedter-Homscheidt, M., Hoyer-Klick, C., Killius, N., Betcke, J., Lefevre, M., Wald, L., Wey, E., and Saboret, L., 2018, "User's Guide to the CAMS Radiation Service," Copernicus Atmosphere Monitoring Service, https://atmosphere.copernicus.eu/sites/default/files/2022-01/CAMS2_73_2021SC1_D3.2.1_2021_UserGuide_v1.pdf

[13] Laguarda, A. and Abal, G., 2019, "Assessment of empirical models to estimate UV-A, UV-B and UV-E solar irradiance from GHI," *Proceedings of the ISES Solar World Congress 2019*, Santiago de Chile, Chile, 4–7 November, 2019, https://proceedings.ises.org/?conference=swc2019&doi=10.18086%2Fswc.2019.42.04

[14] Habte, A., Sengupta, M., Gueymard, C. A., Narasappa, R., Rosseler, O., and Burns, D. M., 2019, "Estimating Ultraviolet Radiation From Global Horizontal Irradiance," IEEE Journal of Photovoltaics, **9**(1), pp. 139–146.

[15] Iqbal, M., 1983, *An introduction to solar radiation*, Academic Press, New York, USA.

[16] Burrows, J. P., Richter, A., Dehn, A., Deters, B., Himmelmann, S., Voigt, S., and Orphal, J., 1999, "Atmospheric remote-sensing reference data from GOME-2. Temperature-dependent absorption cross sections of O_3 in the 231–794 nm range," J. Quant. Spectrosc. Radiat. Transfer, **61**(4), pp. 509–517.

[17] Peel, M. C., Finlayson, B. L., and McMahon, T. A., 2007, "Updated world map of the Köppen-Geiger climate classification," Hydrology and Earth System Sciences, **11**(5), pp. 1633–1644.

[18] Stoffel, T. and Andreas, A., 1981, "NREL Solar Radiation Research Laboratory (SRRL): Baseline Measurement System (BMS)," NREL Report No. DA-5500-56488, doi: http://dx.doi.org/10.5439/1052221.

[19] McArthur, L., 2005, "Baseline Surface Radiation Network Operations manual," World Climate Research Programme - WMO, Tech. Rep. WCRP-121/ WMO TD-No. 1274.

[20] Gelaro, R., McCarty, W., Suârez, M., Todling, R., Molod, A., Takacs, L., Randles, C., Darmenov, A., Bosilovich, M., Reichle, R., and Wargan, K., 2017, "The Modern-Era RetrospectiveAnalysis for Research and Applications, Version 2 (MERRA-2)," Journal of Climate, **30**(14), pp. 5419–5454.

[21] Laguarda, A., 2021, "Modelado de la irradiancia solar sobre la superficie terrestre: Modelos físicos e híbridos utilizando información satelital sobre la Pampa Húmeda," Ph.D. thesis, Facultad de Ingeniería, Universidad de la República, Montevideo, Uruguay, https://www.colibri.udelar.edu.uy/jspui/handle/20.500.12008/9440/browse?type=subject&order=ASC&rpp=20&value=Modelos+satelitales

[22] Young, A., 1994, "Air mass and refraction," Applied Optics, **33**(6), pp. 1108–1110.

[23] Zhang, J., Florita, A., Hodge, B.-M., Lu, S., Hamann, H. F., Banunarayanan, V., and Brockway, A. M., 2015, "A suite of metrics for assessing the performance of solar power forecasting," Solar Energy, **111**, pp. 157–175.

[24] Espinar, B., Ramírez, L., Drews, A., Beyer, H. G., Zarzalejo, L. F., Polo, J., and Marín, L., 2009, "Analysis of different comparison parameters applied to solar radiation data from satellite and German radiometric stations," Solar Energy, **83**(1), pp. 118–125.

[25] Long, C. and Shi, Y., 2008, "An Automated Quality Assessment and Control Algorithm for Surface Radiation Measurements," The Open Atmospheric Science Journal, **2**, pp. 23–37.

Appendix A: Modeling the UVA band

The methodology described in Section 3 is applied to the UVA radiation band (315–400 nm) at the LES and GCO sites, where this measurement was available (Table 3). UVA from the PIL site had some systematic error and was excluded from the analysis. Because ozone is not expected to play a significant role in the UVA band [13], the parametrizations are independent of the ozone content: i.e., $b_5 = 0$, $b_6 = 0$ in Eq. (3) and $a_3 = 0$ in Eq. (2) for all sites[5].

Table 8 UVA coefficients per site. The last two columns show the (weighted) average coefficients and their respective standard deviations using the weights listed in the last row.

Model	Coefficient	LES	GCO	Average	σ
CT	c_0	0.054	0.055	**0.055**	0.000
NP0	b_0	0.072	0.064	**0.067**	0.004
	b_1	-0.020	-0.005	**-0.011**	0.007
	$b_2 \times 10^2$	0.626	-0.090	**0.217**	0.354
	$b_3 \times 10^3$	-0.946	0.366	**-0.196**	0.649
	$b_4 \times 10^4$	0.549	-0.275	**0.078**	0.408
PM0	a_0	0.053	0.055	**0.054**	0.001
	a_1	-0.244	-0.219	**-0.230**	0.012
	a_2	-0.221	-0.190	**-0.203**	0.015
	# data pairs	59185	78928	-	-
	Weights on average	0.429	0.571	-	-

Following the same random sampling and cross-validation procedure, a set of coefficients and performance indicators for each site is obtained. Table 8 shows the locally adjusted coefficients for each model and site. The last rows show the number of data pairs and the weights for each site. The last columns show the (weighted) average coefficients and their standard deviations. These sets of coefficients are used to construct the average versions for each model. For instance, the average PM model for UVA fraction is:

$$f_A = 0.054 \times k_t^{-0.230} \times m^{-0.203}. \tag{A1}$$

When this and the other models are evaluated, the performance indicators in Table 9 are found.

The performance of the locally adjusted models at each site is shown as filled bars in Figure 7. The performance of the average models is shown with hatched bars. For all models, a small increase in RMSD is associated with the use of a single set of coefficients (average model). The performance indicators of the average models are listed (in relative terms) in Table 9. As with other variables, PM0 is the best model, both as a local model and as an average model. A very good overall performance is obtained from its average version: 6.5% of rRMSD and negligible bias.

Finally, Figure 8 shows the scatter plots for the NP0 and PM0 average model estimations of UVA for the LES site. Note the smaller scatter associated with the PM0 model and the tendency to overestimate at high irradiance values.

---

[5]We also tested an ozone-dependent PM model, and it provided no significant gain over PM0.

Table 9 Average model performance for UVA. The simple average of the relative indicators is shown in the last column. Weighted averages are calculated with the weights from Table 8, and relative indicators are percentages of the average measured values indicated in the last row.

Model	Metric	LES	GCO	Average
CT	rMBD (%)	1.9	0.1	**0.9**
	rRMSD (%)	10.6	11.2	**10.9**
	KSI (%)	2.9	2.0	**2.4**
NP0	rMBD (%)	0.8	-2.3	**-1.0**
	rRMSD (%)	9.4	9.5	**9.5**
	KSI (%)	4.4	3.3	**3.8**
PM0	rMBD (%)	2.2	-1.8	**-0.1**
	rRMSD (%)	5.6	7.1	**6.5**
	KSI (%)	2.3	1.8	**2.1**
$\langle I_{UVA} \rangle$	(W/m^2)	24.4	23.6	**23.9**

Appendix B: Details of the ground measurements quality control procedure

To achieve reliable and accurate results, a systematic approach to quality control is imperative. The initial step in this process is data preprocessing, where adjustments are made to the temporal attributes and sampling frequency. Following the World Meteorological Organization guidelines, time tags are standardized to UTC-0, and labels are aligned with the start of each interval. The sample frequency is unified to 10-minute intervals, resampling the 1-minute data with averages for 10 minutes. Missing data are ignored in this step. Using the metadata for each site, the cosine of the solar zenith angle, $\cos\theta_z$, is calculated at mid-interval points using routines from the PVlib library in Python.

An expert visual inspection is conducted in the five datasets to to detect obvious anomalies. Finally, the five 10-minute datasets are subjected to a semiautomated quality control procedure based on eight filters applied on the variables GHI, UVA, UVB, and UVE and their combinations, as described in Table 10. Filter F1 restricts data records to those with solar altitudes larger than 7°, thus minimizing the incidence of the cosine error and other special conditions that occur near sunrise and sunset. The other filters are lower and upper boundaries inspired in the BSRN filtering procedure [25]. Filters F3, F4, and F5 apply to the three UV fractions, whereas F2, F6, and F7 apply to GHI, UVA, and UVB, normalized by the respective scale factors S_0, S_A, and S_B. This set of filters is applied to each dataset, using a specific set of parameters for each site and variable. The parameters are selected visually by inspecting figures such as Figure 9, and their values are listed in tables 11 to 15, with the filtering results. In summary, all the training and validation sets (GHI, UVX) are the result of applying F1 and F2 filters, along with additional conditions imposed according to the UV component considered; i.e., F3 and F6 for UVA, F4 and F7 for UVB, and F5 for UVE (see Table 3).

The average number of records that pass the relevant filters can be used as a raw indicator of the average quality of each dataset. Three sites (LES, GCO, and GWN) are well above 90%, whereas the other two sites (ATM and PIL) are below 86%. After filter F2 is applied, a few low values of GHI remain in the datasets. Because the UV fractions are very sensitive to low GHI, these were removed through the additional condition $GHI > 15\,\text{W/m}^2$.

Table 10 Description of filters applied to all datasets. The UV fractions are $f_A = UVA/GHI$, $f_B = UVB/GHI$ and $f_E = UVE/GHI$. Scale factors are applied to f_B AND f_E in F4 and F5. The solar constant used in F2 is $S_0 = 1361\,\text{W/m}^2$, and the scaling factors for UVA and UVB (used in F7 and F8) are $S_A = 100\,\text{W/m}^2$ and $S_B = 10\,\text{W/m}^2$, respectively.

Filter	Short description	Condition	Variables
F1	Minimum solar altitude	$\cos\theta_z > 0.12$	All
F2	Boundaries for GHI	$c_1 \leq \frac{GHI}{S_0} \leq c_2 + f_2 \cdot (\cos\theta_z)^{a_2}$	GHI
F3	Boundaries for UVA fraction	$c_1 \leq f_A \leq c_2$	UVA, GHI
F4	Boundaries for UVB fraction	$c_1 + f_1 \cdot (\cos\theta_z)^{a_1} \leq f_B \times 10^3 \leq c_2 + f_2 \cdot (\cos\theta_z)^{a_2}$	UVB, GHI
F5	Boundaries for UVE fraction	$c_1 + f_1 \cdot (\cos\theta_z)^{a_1} \leq f_E \times 10^4 \leq c_2 + f_2 \cdot (\cos\theta_z)^{a_2}$	UVE, GHI
F6	Boundaries for UVA	$c_1 \leq \frac{UVA}{S_A} \leq c_2 + f_2 \cdot (\cos\theta_z)^{a_2}$	UVA
F7	Boundaries for UVB	$c_1 \leq \frac{UVB}{S_B} \leq c_2 + f_2 \cdot (\cos\theta_z)^{a_2}$	UVB

Table 11 Coefficients and results for site LES. After visual inspection, from 68444 diurnal records, 61833 pass the solar altitude filter (F1). The relative results are expressed as a percentage of these 61833 records. All coefficients are dimensionless. On average, 98.2% of the records pass the filters.

Filter	Variables	c_1	f_1	a_1	c_2	f_2	a_2	Pass	% F1
F2	GHI	0.002	•	•	0.074	1.0	1.2	61213	99.0
F3	GHI, UVA	0.020	•	•	0.2	•	•	60295	97.5
F4	GHI, UVB	0.070	2.2	1.6	2.5	2.0	1.5	59574	96.3
F5	GHI, UVE	0.300	1.8	1.4	3.5	1.7	1.5	59859	96.8
F6	UVA	0.100	•	•	0.017	0.7	1.3	61383	99.3
F7	UVB	0.000	•	•	0.002	0.35	2.1	61367	99.2

Table 12 Coefficients and results for site ATM. After visual inspection, from 32136 diurnal records, 29005 pass the solar altitude filter (F1). The relative results are expressed as a percentage of these 29005 records. All coefficients are dimensionless, and only filters for existing variables (GHI, UVB) are shown. On average, 85.7% of the records pass the filters.

Filter	Variables	c_1	f_1	a_1	c_2	f_2	a_2	Pass	% F1
F2	GHI	0.002	•	•	0.074	1.0	1.2	24872	85.8
F4	GHI, UVB	0.070	2.2	1.6	2.5	2.0	1.5	24749	85.3
F7	UVB	0.000	•	•	0.002	0.264	1.8	24918	85.9

Table 13 Coefficients and results for site GCO. After visual inspection, from 105549 diurnal records, 94244 pass the solar altitude filter (F1). The relative results are expressed as a percentage of these 94244 records. All coefficients are dimensionless. On average, 97.9% of the records pass the filters.

Filter	Variables	c_1	f_1	a_1	c_2	f_2	a_2	Pass	% F1
F2	GHI	0.002	•	•	0.074	1.0	1.2	94117	99.9
F3	GHI, UVA	0.020	•	•	0.2	•	•	94144	99.9
F4	GHI, UVB	0.0	1.45	1.6	2.5	1.6	1.5	93943	99.7
F5	GHI, UVE	0.0	1.8	1.9	1.8	3.5	1.1	94077	99.8
F6	UVA	0.0	•	•	0.005	0.8	1.2	94190	99.9
F7	UVB	0.0	•	•	0.002	0.253	2.0	94127	99.9

Table 14 Coefficients and results for site GWN. After visual inspection, from 105548 diurnal records, 95069 pass the solar altitude filter (F1). The relative results are expressed as a percentage of these 95069 records. All coefficients are dimensionless, and only filters for existing variables (GHI, UVE) are shown. On average, 98.7% of the records pass the filters.

Filter	Variables	c_1	f_1	a_1	c_2	f_2	a_2	Pass	% F1
F2	GHI	0.002	•	•	0.074	1.0	1.2	93820	98.7
F5	GHI, UVE	0.050	1.9	1.9	3.5	1.7	1.5	93713	98.6

Table 15 Coefficients and results for site PIL. After visual inspection, from 98893 diurnal records, 89344 pass the solar altitude filter (F1). The relative results are expressed as a percentage of these 89344 records. All coefficients are dimensionless. On average, 80.4% of the records pass the filters.

Filter	Variables	c_1	f_1	a_1	c_2	f_2	a_2	Pass	% of F1
F2	GHI	-0.002	•	•	0.026	1.0	1.2	81319	91.0
F3	GHI, UVA	0.025	•	•	0.175	•	•	69766	78.1
F5	GHI, UVE	0.100	2.0	2.0	2.000	3.0	1.5	66458	74.4
F6	UVA	0.000	•	•	0.004	0.9	1.2	69794	78.1
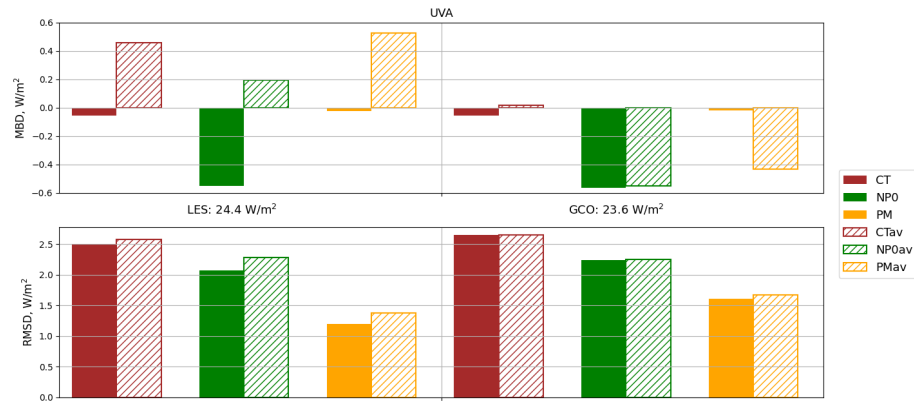
Fig. 7 Performance indicators (MBD and RMSD) for UVA models without ozone. The site-specific models (filled bars) use the coefficients from Table 8, and the average models (hatched bars) use the average coefficients listed in the same table. The measurement average for each site is indicated between both panels.

(*a*) NP

(*b*) PM
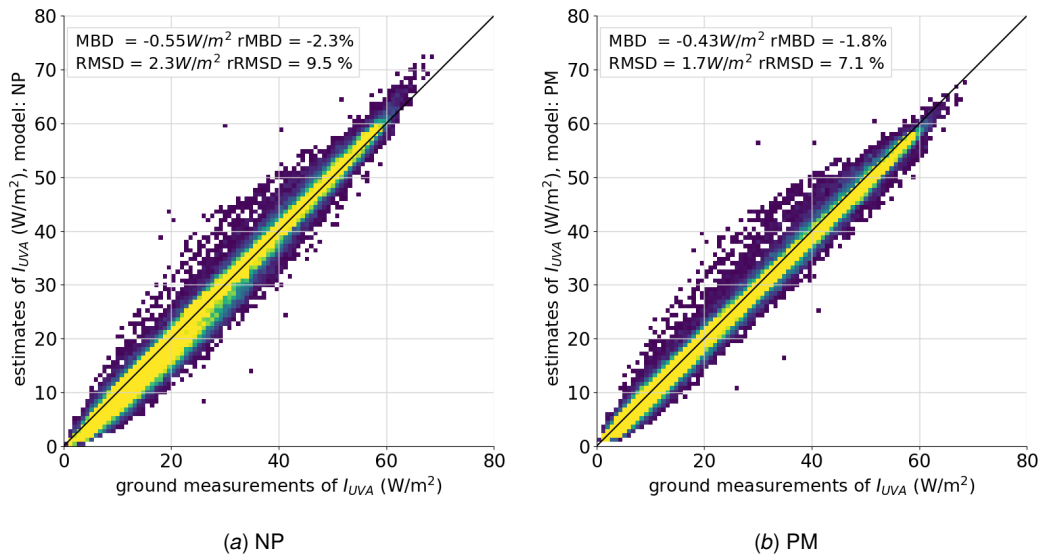
Fig. 8 Scatter plots of UVA estimates using NP and PM average models for the GCO site.
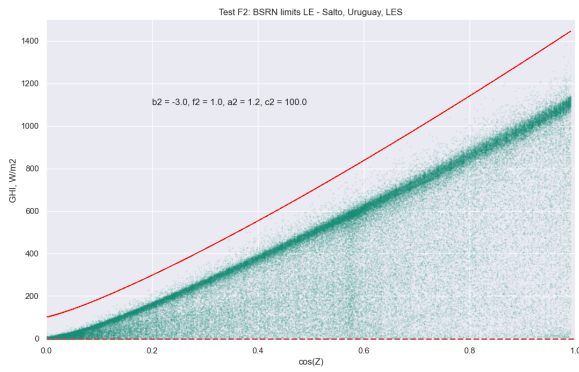
(*a*) Boundaries on GHI from F2
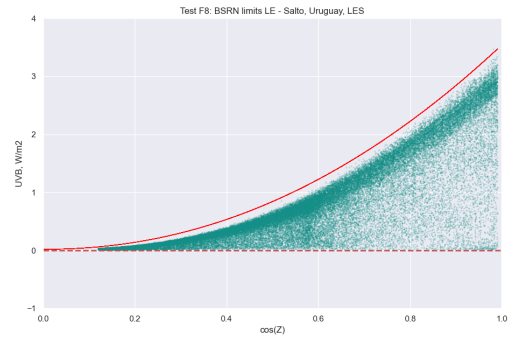
(*b*) Boundaries on UVB from F7
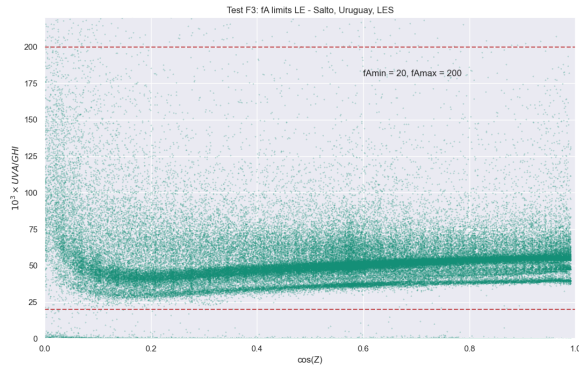
(*c*) Boundaries in f_A from F3
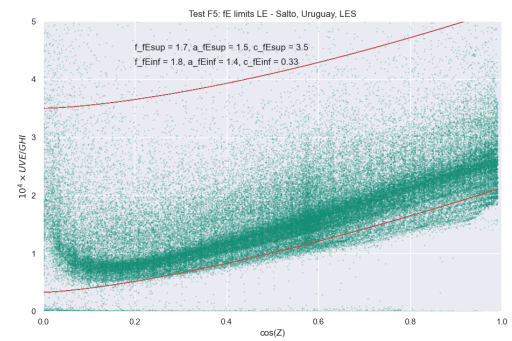
(*d*) Boundaries on f_E from F5

Fig. 9   Boundaries for several variables at the LES site.

List of Figures

List of Tables